論文 / 著書情報
Article / Book Information

Title	X-ray diffraction study on a (111)-textured palladium thin film under hydrogen loading and unloading: film structure evolution and its mechanism
Authors	Takashi Harumoto, Yuichi Suzuki, Ji Shi, Yoshio Nakamura
Citation	J. Appl. Cryst., Vol. 50, 5, pp. 1478–1489
Pub. date	2017, 10
DOI	http://dx.doi.org/10.1107/S1600576717012638

JOURNAL OF APPLIED CRYSTALLOGRAPHY

ISSN: 1600-5767
journals.iucr.org/j

X-ray diffraction study on a (111)-textured palladium thin film under hydrogen loading and unloading: film structure evolution and its mechanism

Takashi Harumoto, Yuichi Suzuki, Ji Shi and Yoshio Nakamura

J. Appl. Cryst. (2017). **50**, 1478–1489

JOURNAL OF APPLIED CRYSTALLOGRAPHY
ISSN 1600-5767

X-ray diffraction study on a (111)-textured palladium thin film under hydrogen loading and unloading: film structure evolution and its mechanism

Takashi Harumoto,[a]* Yuichi Suzuki,[b] Ji Shi[a] and Yoshio Nakamura[a]

[a]Department of Materials Science and Engineering, Tokyo Institute of Technology, 2-12-1 O-okayama, Meguro-ku, Tokyo, 152-8552, Japan, and [b]Materials Analysis Division, Tokyo Institute of Technology, 2-12-1 O-okayama, Meguro-ku, Tokyo, 152-8552, Japan. *Correspondence e-mail: harumoto.t.aa@m.titech.ac.jp

Received 9 June 2017
Accepted 3 September 2017

Edited by A. Borbély, Ecole National Supérieure des Mines, Saint-Etienne, France

Keywords: hydrogen; palladium; diffraction stress analysis; *in situ* X-ray diffraction; structure evolution.

Supporting information: this article has supporting information at journals.iucr.org/j

The incorporation of hydrogen normally results in degradation when applied to metals. In this diffraction study, however, improvement of the film structure, such as in-plane grain growth, lattice defect removal and texture enhancement, was observed in a (111)-textured palladium thin film during hydrogen loading and unloading cycles. Accordingly, diffraction stress analysis was performed to investigate the evolution mechanism. It was found that the formation of the β phase during the α-to-β phase transformation occurred at the same in-plane stress present in the α phase, and *vice versa*. This suggests that the cyclic α–β grain boundary motion during the transformation occurred mainly along the in-plane direction, contributing to the film structure evolution.

1. Introduction

It is well known that hydrogen incorporation into metals results in hydrogen embrittlement (Kirchheim & Pundt, 2014). For this reason, hydrogen is considered one of the most harmful elements with respect to metals. However, during the past few decades, several researchers have identified hydrogen as a useful element for certain processes. For instance, the hydrogen absorption–desorption-based grain refinement method, known as hydrogenation–decomposition–desorption–recombination (HDDR), is employed for improving the magnetic properties of neodymium–iron–boron-based magnets (Harris & McGuiness, 1991; Nakayama & Takeshita, 1993). Grain refinement by HDDR can also enhance the mechanical and electrical properties of copper alloys (Iwaki *et al.*, 2009; Okada *et al.*, 2010). In addition, hydrogen incorporation promotes interdiffusion, known as 'hydrogen-induced lattice mobility' (Sidorenko *et al.*, 1978; Noh *et al.*, 1991, 1992; Flanagan & Noh, 1995; Watanabe *et al.*, 1996; Hayashi *et al.*, 1998). Furthermore, in the case of 304 and 316L austenitic stainless steels, hydrogen may improve resistance against fatigue crack growth (Murakami *et al.*, 2010).

Although these investigations have been conducted intensively on bulk materials, few reports have been made on thin films. According to Gremaud *et al.* (2009) and Pivak *et al.* (2011), hydrogen has been shown to improve (111)-textured palladium (Pd) thin films: hydrogen loading and unloading results in an enhancement of the (111) texture and an increase in crystal size (hereafter, these are denoted as film structure evolution). However, since those papers focused on the hydrogenography, they presented no information about the film structure during phase transformation from the dilute

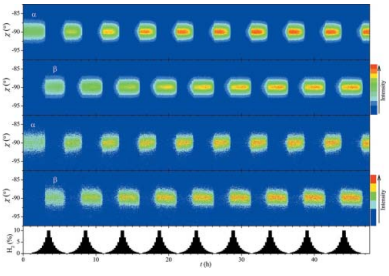

palladium hydride α phase to the palladium hydride β phase at higher hydrogen concentration. Therefore, the mechanism of film structure evolution is still unclear and further investigation is required.

In this study, we try to reveal its mechanism by performing an *in situ* X-ray diffraction (XRD) study on a (111)-textured Pd thin film under α-to-β and β-to-α phase transformations. Since we measured the diffracted X-rays using a two-dimensional position-sensitive detector at two different tilt angles ($\psi = 0$ and 70.5°), changes such as out-of-plane/in-plane grain sizes, texture, in-plane stress and hydrogen concentration of both the α and β phases could be estimated from the acquired diffraction patterns. The mechanism of film structure evolution is then discussed on the basis of these results.

2. Experimental

A (111)-textured Pd thin film of thickness 48 nm was sputter deposited onto a synthetic fused silica glass substrate coated with an APA underlayer. The APA underlayer consisted of AlN(20 nm)/Pd(8 nm)/AlN(20 nm). As shown in §3.1, the underlayer improved the (111) texture of the Pd film while the diffraction intensity from the underlayer could be ignored. Note that the 8 nm-thick Pd interlayer was employed for preparing the *c*-axis-oriented AlN layer, the surface of which was suitable for face-centred cubic (111) deposition (Harumoto *et al.*, 2013). However, the Pd interlayer had no role and no reaction during hydrogen loading cycles, since it was coated with the AlN layer. This was confirmed by electrical resistivity measurements during the introduction of hydrogen gas (Fig. S1 in the supplementary information): the electrical resistivity of the Pd interlayer in the APA underlayer had no response against the introduced hydrogen gas (compare Figs. S1*a* and S1*c*), while that of a Pd(8 nm)/AlN(20 nm)/substrate exhibited a large resistivity change (Figs. S1*b* and S1*c*).

The multilayer film was deposited using the continuous sputter deposition method, suitable for preparing textured films (Harumoto *et al.*, 2013, 2016). Details of the deposition conditions are described in our previous report (Harumoto *et al.*, 2017). The layer thickness and the roughness of the multilayer film were confirmed by X-ray reflectometry (XRR). The experimental details of the XRR measurement setup and the curve fitting were reported by Harumoto *et al.* (2014). The layer structure of the film was analysed using Auger electron spectroscopy (AES) (JAMP-9500F; JEOL, Tokyo, Japan). The film surface was irradiated with 10 keV electrons. The depth profile was acquired using an argon (Ar) sputter gun (Ar ion energy: 2 keV; sputtering rate: 13.6 nm min^{-1} for SiO_2). The surface morphology of the film was investigated using atomic force microscopy (AFM) (AFM5100N; Hitachi High-Technologies, Tokyo, Japan) with the instrument in a dynamic force microscope mode.

For the diffraction study, a D8 Discover X-ray diffractometer (Bruker AXS, Karlsruhe, Germany) was used. The diffractometer was equipped with a rotating copper (Cu) anode X-ray generator, cross-coupled multilayer mirrors for the Cu $K\alpha$ radiation (0.15418 nm) with a 0.1 mm-diameter pinhole exit collimator, a goniometer and a two-dimensional position-sensitive detector (Vantec-500) placed 199 mm from the centre of the goniometer. The beam divergence of the X-rays after the mirrors was less than 0.04° in both horizontal and vertical directions. To stabilize the diffractometer, the X-ray generator was turned on at normal conditions (50 kV, 22 mA) for 24 h before the actual measurement. Since (111)-textured Pd films exhibit a strong 111_{Pd} diffraction intensity at tilt angles $\psi = 0$ and 70.5°, two-dimensional patterns were acquired at these two ψ angles alternately. The acquisition time for each frame was 50 s. The specimen was rocked in an angular width of ±2° from the centre angle. During the entire *in situ* measurement of 47.6 h, no move command was applied to the diffraction angle (2θ) axis. A hydrogen (H_2) and nitrogen (N_2) gas mixture was introduced into a gas cell designed by ourselves (Harumoto *et al.*, 2017). Hydrogen gas was introduced in cycles up to 10%. The actual H_2 gas profile is shown later, together with the diffraction results. Note that by using two mass flow controllers the total flow of the gas mixture was kept constant. The temperature and pressure during the measurement were room and atmospheric, respectively.

Line profiles were extracted from the two-dimensional patterns. The profiles were analysed using peak profile fitting conducted with *Mathematica* (Version 9; Wolfram, Champaign, IL, USA). During the fitting, the peak was assumed to consist of two Lorentzian profiles (Cauchy curves) that correspond to Cu $K\alpha_1$ and Cu $K\alpha_2$ peaks. The accuracy and the instrumental broadening of the diffractometer were estimated using NIST SRM 640c silicon powder. The accuracy of the diffraction angle 2θ was better than 0.04° at both ψ angles. Errors were estimated from the sum of the accuracy of the diffractometer and the standard error of the peak fitting.

3. Results and discussion

3.1. Film structure

Fig. 1 shows the out-of-plane diffraction line profiles of the Pd(48 nm)/APA underlayer/substrate and the APA underlayer/substrate. For comparison, the profiles of the Pd(48 nm)/substrate and the silica glass substrate itself are also shown. It is clear that the Pd thin film on the APA underlayer is highly (111) textured: strong 111_{Pd} and 222_{Pd} peaks were detected while other *hkl* peaks were almost absent in the profile of the Pd(48 nm)/APA underlayer/substrate (on closer examination, however, there is a very small trace of the 200_{Pd} peak). The Pd film without the APA underlayer [Pd(48 nm)/substrate] exhibited small 111_{Pd} and 200_{Pd} peaks, indicating weak (111) and (100) textures. The diffraction profile of the APA underlayer/substrate exhibits very weak 002_{AlN} and 111_{Pd} peaks; however, its 111_{Pd} intensity was negligible compared with the Pd film on the APA underlayer. Thus, although the APA underlayer contains a Pd layer, it does not affect our diffraction study on highly (111)-textured Pd thin films. Note that we also confirmed that there was no change in the diffraction profile of the APA underlayer during hydrogen loading and unloading.

The layer thickness and roughness of the Pd(48 nm)/APA underlayer/substrate were confirmed by XRR (Fig. 2). The simulated curve exhibits a good agreement with the experimental one. The best-fit result is shown in the inset of Fig. 2, indicating that the measured layer thickness of each layer is almost equal to the designed one, although the AlN layers exhibit small deviations. Also, the surface/interface roughnesses were of sub-nanometre order, showing the smoothness of the surface/interfaces.

The layer structure was analysed using the AES depth profile (Fig. 3*a*), confirming the designed layer structure of the Pd(48 nm)/APA underlayer/substrate. Also, no oxygen contamination was detected at the interfaces. The depth profile of the film after the cyclic hydrogen loading and unloading is shown in Fig. 3(*b*). There was no change in the depth profiles. Thus, the layer structure seems to have resistance to the hydrogen loading and unloading cycles. Note that the difference in the sputtering rate between two depth profiles seems to have originated from the instability of the Ar gun employed for sputtering.

The surface morphology of the Pd(48 nm)/APA underlayer/substrate is shown in Fig. 4(*a*). The in-plane isotropy is confirmed and the in-plane grain size is around 20 nm. The

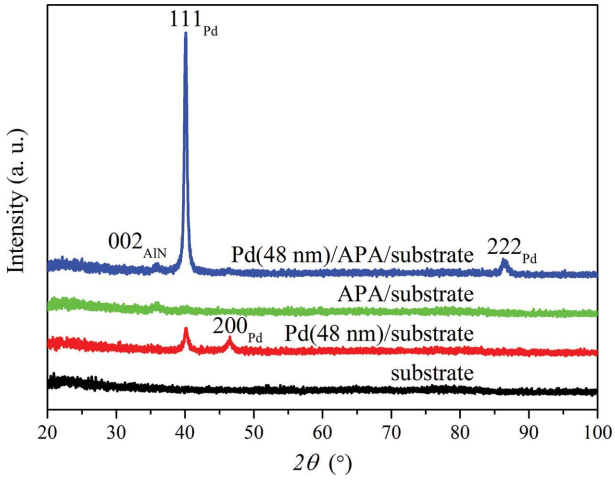

Figure 1
Out-of-plane diffraction line profiles of the Pd(48 nm)/APA underlayer/substrate, APA underlayer/substrate, Pd(48 nm)/substrate and substrate itself. In this figure, the APA underlayer is abbreviated to 'APA'.

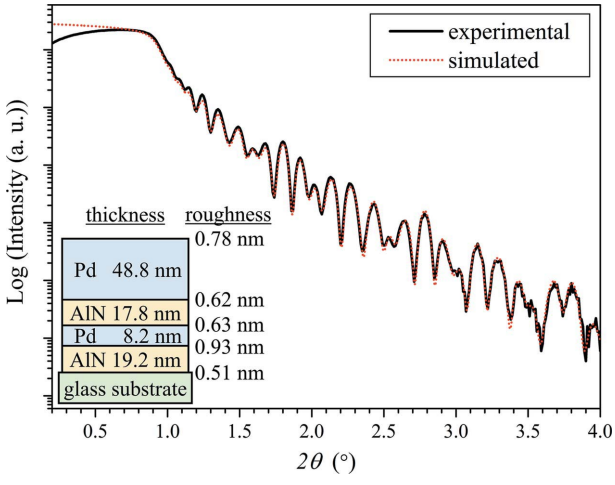

Figure 2
XRR curve of the as-deposited Pd(48 nm)/APA underlayer/substrate. The simulated curve was calculated using the best-fit values shown in the inset.

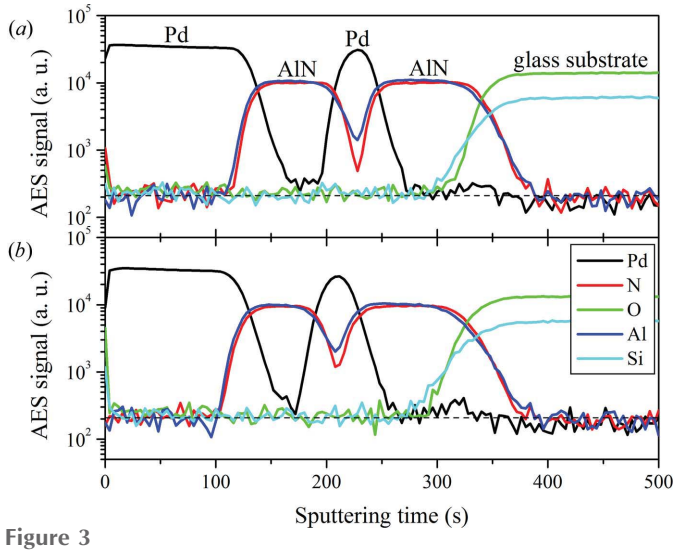

Figure 3
AES depth profiles of the Pd(48 nm)/APA underlayer/substrate, (*a*) as deposited and (*b*) after the *in situ* XRD measurement (after nine cycles of 10% hydrogen loading). The dashed lines in the figures denote the noise level of the AES signal.

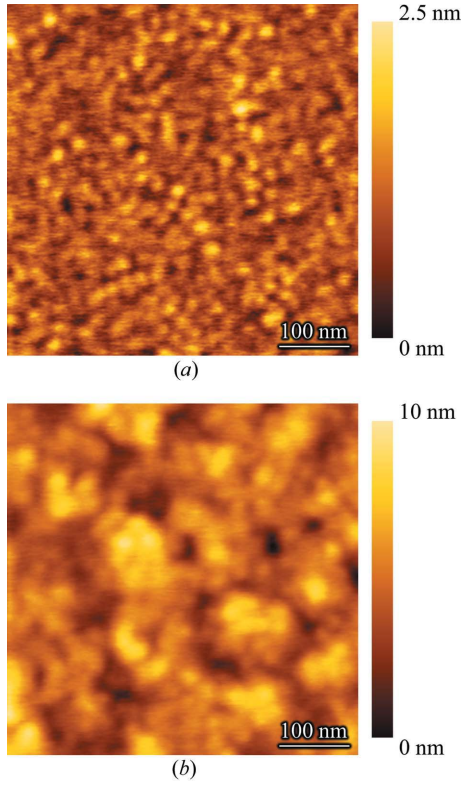

Figure 4
AFM images of the Pd(48 nm)/APA underlayer/substrate, (*a*) as deposited and (*b*) after the *in situ* XRD measurement (after nine cycles of 10% hydrogen loading).

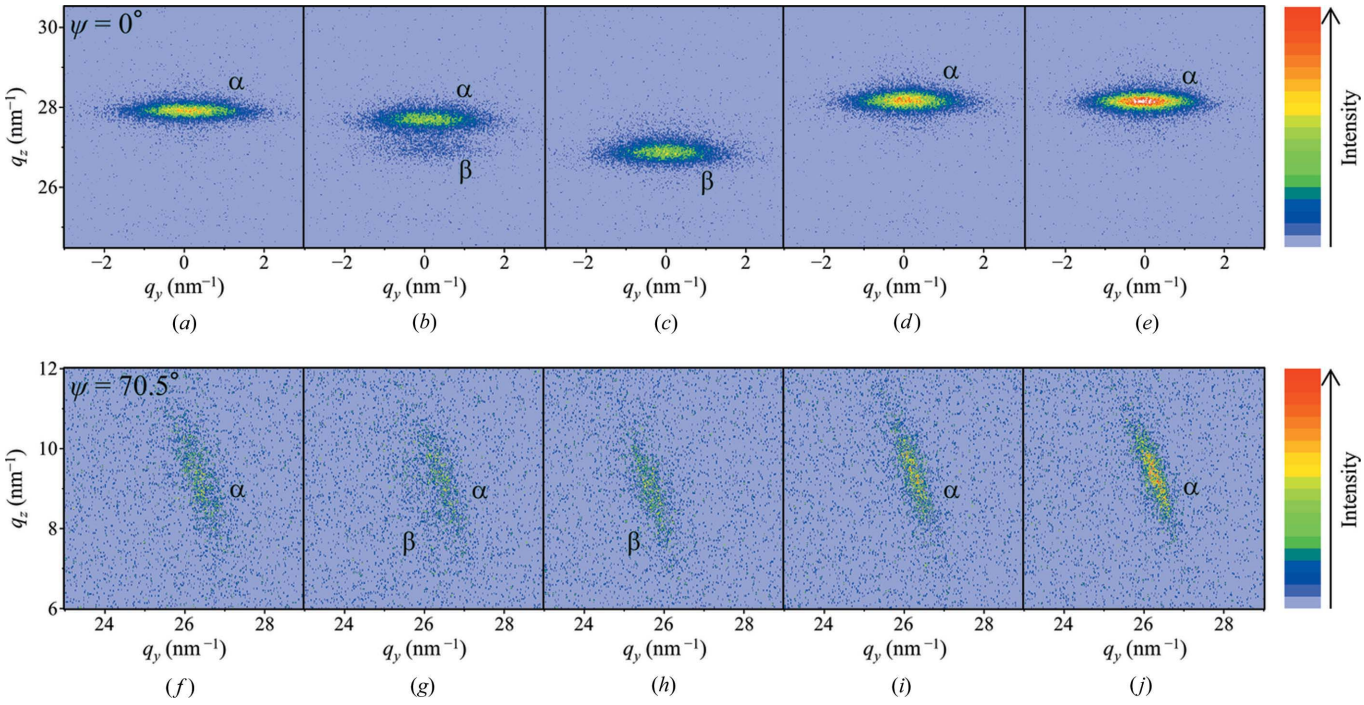

Figure 5
Typical reciprocal space maps calculated from the acquired two-dimensional diffraction patterns: (*a*), (*f*) as deposited (time t = 0 h), (*b*), (*g*) during the initial 4.9% H_2 gas introduction (t = 3.0 h), (*c*), (*h*) during the initial 10% H_2 gas introduction (t = 3.5 h), (*d*), (*i*) after the initial H_2 loading and unloading (t = 6.1 h), and (*e*), (*j*) after nine cycles of hydrogen loading and unloading (t = 47.6 h). The upper row shows the frames at $\psi = 0°$ and the lower shows $\psi = 70.5°$. q_z and q_y are the scattering vectors along the out-of-plane and in-plane directions, respectively. The labels α and β denote the 111 spots of the α and β phases. Regarding t, refer to Fig. 8(*c*).

surface roughness is 0.31 nm (r.m.s.), indicating the very smooth surface. Note that the difference between the roughnesses measured using XRR (0.78 nm) and AFM (0.31 nm) could be explained by the different measurement methods. Fig. 4(*b*) is the AFM image after the *in situ* XRD measurement. An increase in the in-plane grain size (around 30–40 nm) was observed, although the surface roughness also increased (1.48 nm r.m.s.). The mechanism of the in-plane grain growth is discussed later.

In short, it was confirmed that the prepared Pd thin film deposited onto an APA underlayer was highly (111) textured. Since the diffraction intensity from the APA underlayer was very weak, it could be ignored. The surface/interfaces roughnesses were sufficiently small and the thickness of each layer was almost equal to the designed one. Also, because no change in the AES depth profiles was detected, the layer structure was confirmed to be sufficiently stable during hydrogen loading and unloading. We hence conducted the *in situ* X-ray diffraction study with this prepared, highly (111)-textured Pd film (next section).

3.2. *In situ* X-ray diffraction study

Two-dimensional diffraction patterns typical of those acquired are shown in Fig. 5. Only ten frames out of a total of 1988 are shown. q_z and q_y denote the out-of-plane and in-plane scattering vectors, respectively. 111_{Pd} at $\psi = 0°$ was observed at $q_y = 0$ as a spot rather than a ring, indicating the well developed out-of-plane (111) texture (Fig. 5*a*). The texture was further confirmed by the spotty appearance of $11\bar{1}_{Pd}$ on the diffraction pattern at $\psi = 70.5°$ (note, 70.5° is the angle between ⟨111⟩) (Fig. 5*f*). In addition, since $111_{Pd(H)}$ remains as a spot during the α-to-β and β-to-α transformations [in the α-to-β case, Fig. 5(*b*)], the (111) texture remained even

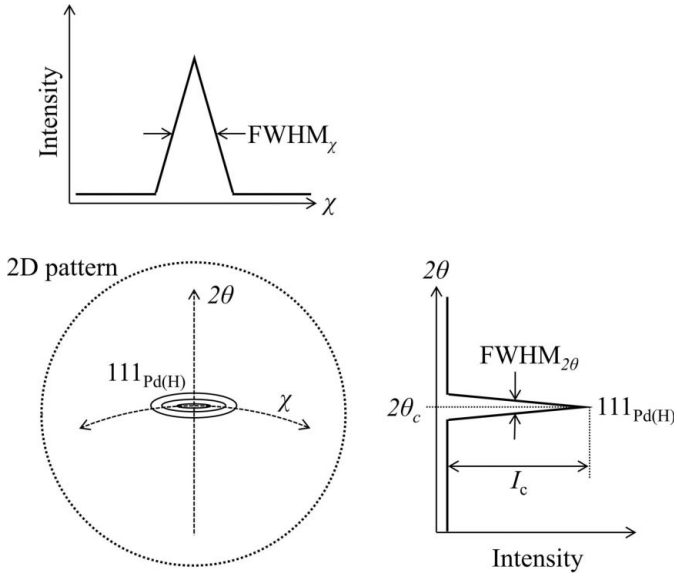

Figure 6
Schematic illustration of 2θ and χ in the two-dimensional pattern and the extraction of line profiles. 2θ_c and I_c denote the peak centre and height of the $111_{Pd(H)}$ peak. $FWHM_{2\theta}$ and $FWHM_\chi$ are the full widths at half-maximum along the 2θ and χ directions, respectively. The centre position of the pattern was (2θ, χ) = (40°, −90°)

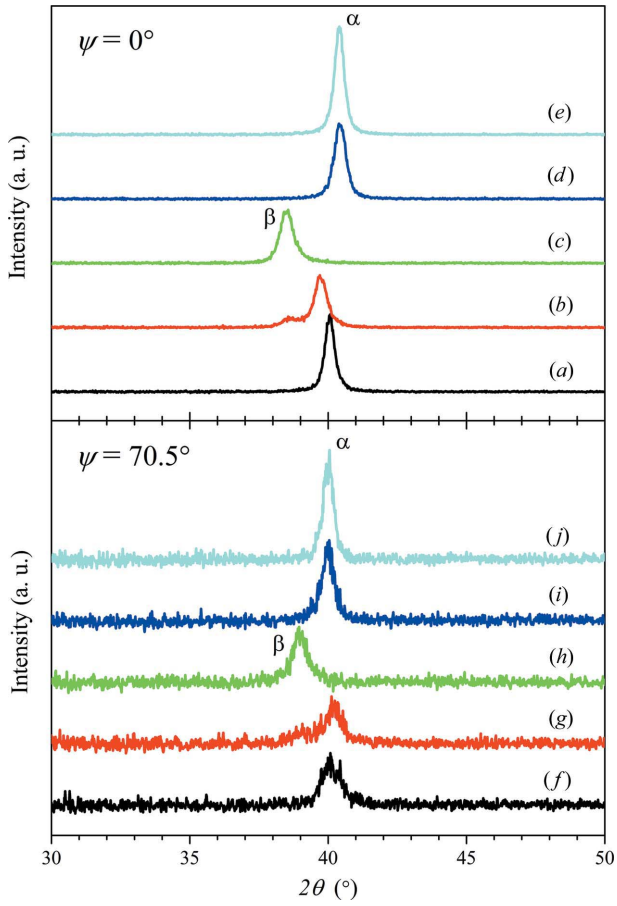

Figure 7
2θ line profiles extracted from the two-dimensional diffraction patterns shown in Fig. 5. (*a*), (*f*) as deposited (time t = 0 h), (*b*), (*g*) during the initial 4.9% H_2 gas introduction (t = 3.0 h), (*c*), (*h*) during the initial 10% H_2 gas introduction (t = 3.5 h), (*d*), (*i*) after the initial H_2 loading and unloading (t = 6.1 h), and (*e*), (*j*) after nine cycles of hydrogen loading and unloading (t = 47.6 h). The labels α and β denote the 111 spots of the α and β phases. Regarding t, refer to Fig. 8(*c*).

after the transformation (compare Figs. 5*a*, 5*b* and 5*c*; Figs. 5*c* and 5*d*; Figs. 5*f*, 5*g* and 5*h*; and Figs. 5*h* and 5*i*). Furthermore, the intensity of 111_{Pd} was increased after the hydrogen loading and unloading cycles (compare Figs. 5*a*, 5*d* and 5*e*, or Figs. 5*f*, 5*i* and 5*j*). It should be noted that the diffractometer was stable enough to analyse the peak intensity (Fig. S2*a* in the supplementary information). Therefore, it was confirmed that the (111) texture remained and film structure evolution took place during the hydrogen loading and unloading cycles.

For further analysis of the measured results, the line profiles along the diffraction angle (2θ) and the detector-tilt angle (χ) were extracted from the two-dimensional diffraction patterns (see the schematic illustration in Fig. 6). Fig. 7 shows the 2θ line profiles extracted from the frames in Fig. 5. The (*a*)–(*j*) labels in Fig. 7 correspond to (*a*)–(*j*) in Fig. 5. During the introduction of H_2 gas, the emergence of the β-phase 111 peak was obviously observed at both $\psi = 0°$ and $\psi = 70.5°$ [Figs. 7(*b*) and 7(*c*) for $\psi = 0°$, and Figs. 7(*g*) and 7(*h*) for $\psi = 70.5°$]. After the hydrogen unloading, a large peak shift was observed at $\psi = 0°$ (compare Figs. 7*a* and 7*d*) while there was only a slight shift at $\psi = 70.5°$ (compare Figs. 7*f* and 7*i*). This difference is related to the substrate clamping effect and the in-plane stress (details are discussed later). In addition to the peak intensity (height) increase, the cyclic hydrogen loadings resulted in a decrease in the peak width (compare Figs. 7*a*, 7*d* and 7*e*, or Figs. 7*f*, 7*i* and 7*j*). This indicates the film structure evolution, such as the grain growth and the removal of defects from the lattice.

Next, the line profiles were compiled into intensity maps against time (Fig. 8 for 2θ and Fig. 9 for χ). The introduced hydrogen gas profile is attached to these figures and those showing subsequent analysis results (Fig. 8*c*, Fig. 9*c*, Fig. 10*e*, Fig. 12*c* and Fig. S2*b*). It is clear that the intensities of the $111_{Pd(H)}$ peaks both at $\psi = 0°$ and at $\psi = 70.5°$ increase with the number of cycles, indicating the film's structural evolution over hydrogen loading and unloading cycles. In Fig. 8(*a*), it is

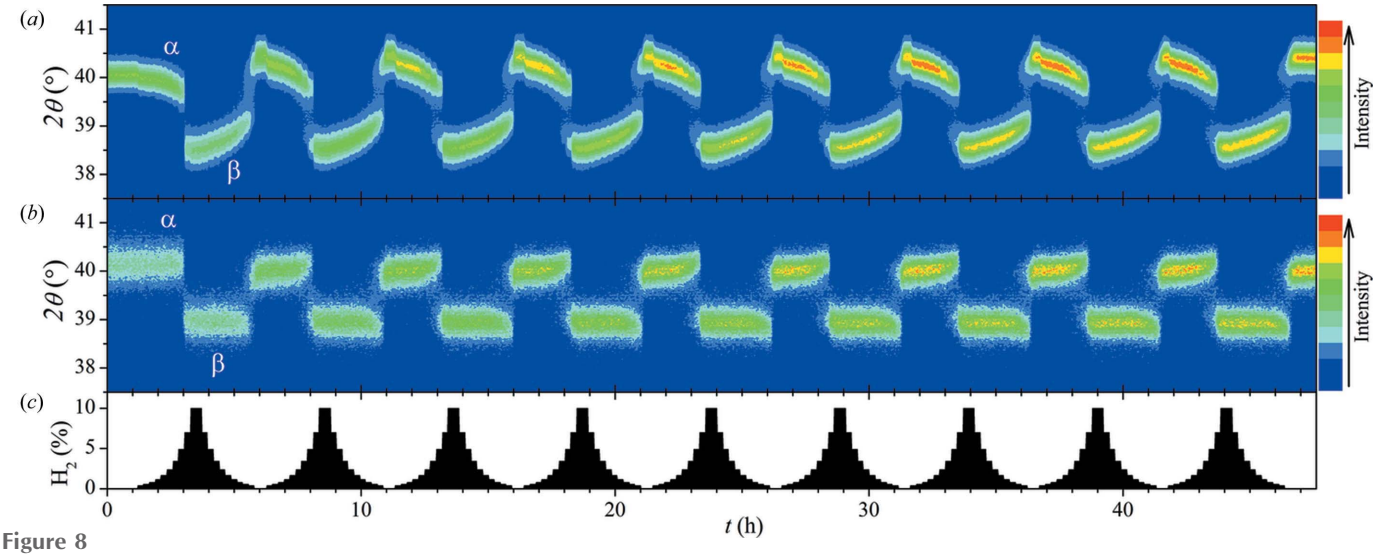

Figure 8
Diffraction intensity maps of the 2θ line profiles at (*a*) $\psi = 0°$ and (*b*) $\psi = 70.5°$ against time (t). The introduced H_2 gas profile is also shown in (*c*). The labels α and β denote the 111 peaks of the α and β phases, respectively.

also clear that the shift of the $111_{Pd(H)}$ peak at $\psi = 0°$ can be divided into two components: one is a continuous peak shift within the same phase and the other is an abrupt large peak shift due to the phase transformation. In contrast, the shift of the $111_{Pd(H)}$ peak at $\psi = 70.5°$ is essentially composed of just the latter component (Fig. 8*b*). This indicates that, except for the phase transformation period, in-plane lattice expansion/shrinkage is suppressed while out-of-plane expansion/shrinkage occurs intensively. This observation is related to the substrate clamping effect, *i.e.* owing to the substrate, the film exhibits an anisotropic expansion/shrinkage (Miceli *et al.*, 1991; Reimer *et al.*, 1993; Zabel & Weidinger, 1995; Laudahn *et al.*, 1999; Pundt & Kirchheim, 2006; Pivak *et al.*, 2011; Wagner *et al.*, 2011; Kirchheim & Pundt, 2014; Callori *et al.*, 2016; Harumoto *et al.*, 2017). According to Figs. 9(*a*) and 9(*b*), the retention of the (111) texture during hydrogen cycling is obvious, since the 111 peaks of both the α and the β phases are observed always at $\chi = -90°$, the centre of the detector-tilt angle. The small peak shift in Fig. 9(*b*) seems to originate from the lattice distortion, or the angle change between [111] and $[11\bar{1}]$, due to the in-plane stress.

The profile fitting results are shown in Fig. 10. Again, a gradual increase in the peak intensity (peak height) was clearly observed for both $\psi = 0°$ and $\psi = 70.5°$ (Fig. 10*a*). Also, the directional dependence of the lattice expansion/shrinkage was confirmed: the 111 peak at $\psi = 0°$ exhibits a relatively dynamic peak shift as compared with the one at $\psi = 70.5°$ (Fig. 10*b*). In addition to the intensity increase and the peak shift, a decrease in the peak full width at half-maximum (FWHM) along the 2θ and χ directions was observed at both $\psi = 0°$ and $\psi = 70.5°$ (Figs. 10*c* and 10*d*). This also indicates the film evolution. In detail, the $FWHM_{2\theta}$ at $\psi = 0°$ corresponds to the out-of-plane crystal size (namely, the crystal thickness) and the lattice defects (Fig. 10*c*, $\psi = 0°$). Similarly, the $FWHM_{2\theta}$ at $\psi = 70.5°$ is related to the crystal size along $\psi = 70.5°$ (corresponding mainly to the in-plane crystal size) and the lattice defects (Fig. 10*c*, $\psi = 70.5°$). At both $\psi = 0°$ and $\psi = 70.5°$, the $FWHM_{2\theta}$ plots of the α phase (also in the case of the β phase) exhibit a U-shaped curve. This suggests that, during the α-to-β and β-to-α phase transformations (*i.e.* during the formation of the new phase and the disappearance of the matrix phase), the crystal size is small and the crystal includes many lattice defects. However, once the transformation is completed, the crystal grows large and the lattice is stabilized. During the initial hydrogen loading cycles, the β-phase plots exhibit a slightly larger $FWHM_{2\theta}$ than the α-phase plots.

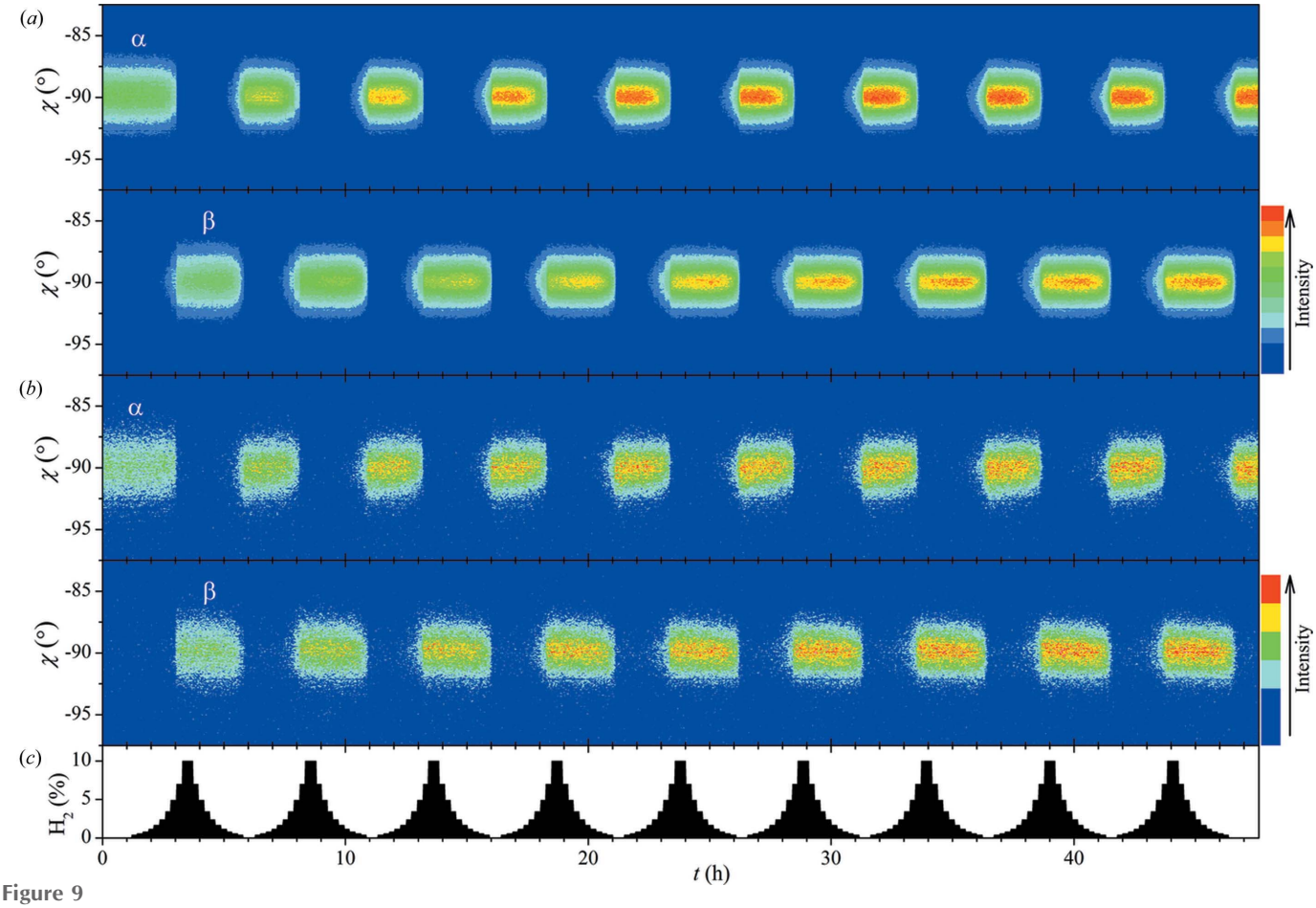

Figure 9
Diffraction intensity maps of χ line profiles at (*a*) $\psi = 0°$ and (*b*) $\psi = 70.5°$ against time (t). Maps of the α and β phases are shown separately. (*c*) shows the introduced H_2 gas profile.

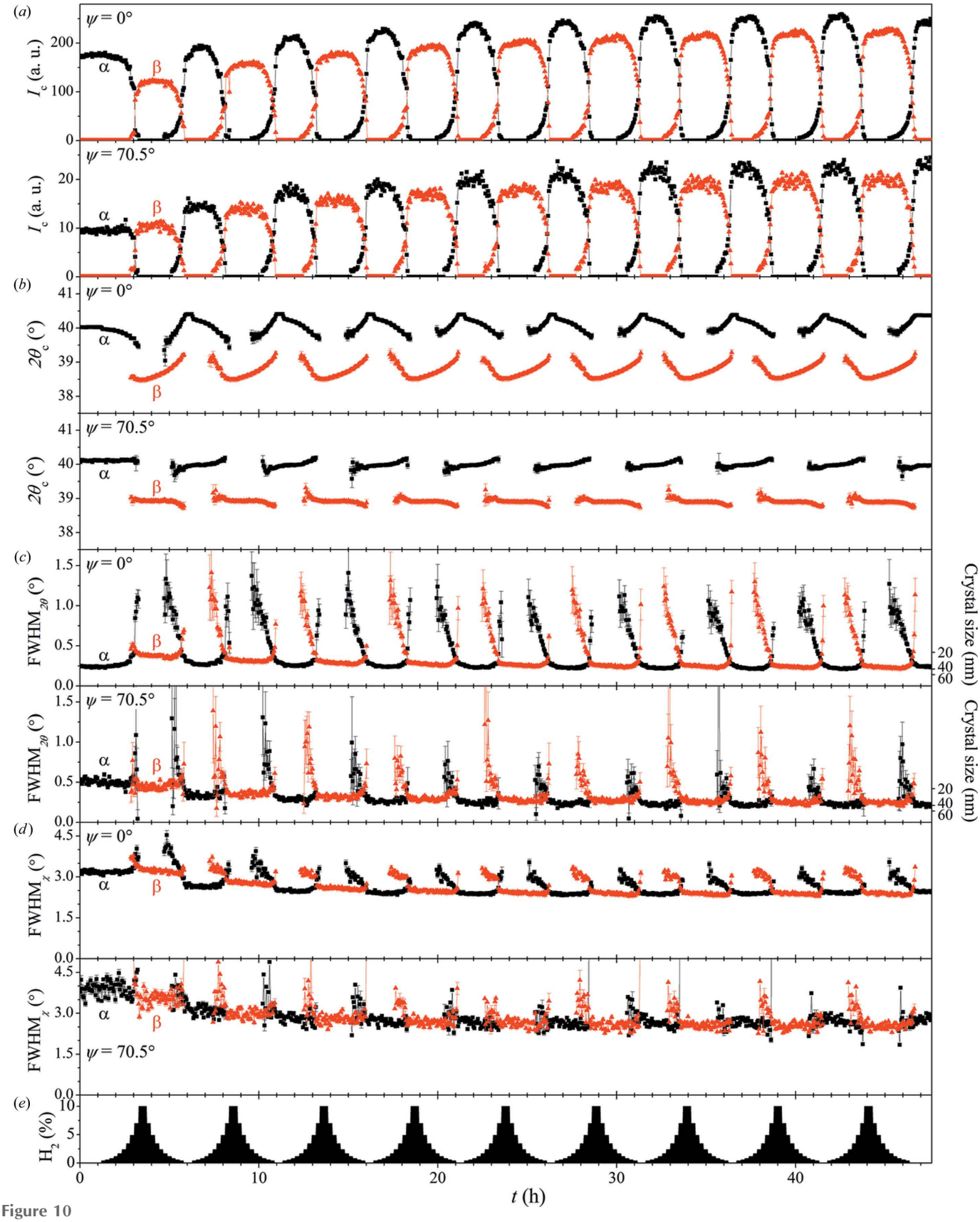

Figure 10
Profile fitting results of the $111_{Pd(H)}$ spots at $\psi = 0$ and 70.5°. (*a*) Peak intensity (peak height) (I_c), (*b*) peak centre position ($2\theta_c$), (*c*) peak FWHM along the 2θ direction (FWHM$_{2\theta}$) and (*d*) peak FWHM along the χ direction (FHWM$_\chi$). The introduced hydrogen gas profile is shown in (*e*). In (*c*), the axis on the right-hand side represents the crystal size estimated from the Scherrer equation. The black square and red triangle plots correspond to the fitting results of the α and β phases, respectively.

However, after several cycles, the β-phase plots reach almost the same $FWHM_{2\theta}$ as that of the α phase. In addition, the $FWHM_{2\theta}$ at the transformation completion becomes smaller as the cycles increase. Thus, many lattice defects would be introduced into the lattice during the initial hydrogen loading cycles (especially during the first β-phase formation), and they would be removed after several cycles. At the same time, grain growth also took place. Under the assumption that there was no peak broadening due to the lattice defects, the $FWHM_{2\theta}$ can be transformed into the crystal size using the Scherrer equation [the right-hand side of Fig. 10(*c*)]. The Scherrer constant was assumed to be 0.9. The crystal thickness was around 30–40 nm as deposited and decreased during the initial hydrogen loadings; however, after several hydrogen loading and unloading cycles, it returned to 30–40 nm (Fig. 10*c*, ψ = 0°). This size is very close to the thickness of the Pd film (48.8 nm) measured using XRR (Fig. 2). The crystal size along ψ = 70.5° was around 20 nm initially and exhibited a gradual increase up to 40 nm after the cycles (Fig. 10*c*, ψ = 70.5°). The same grain size increase from 20 nm to 30–40 nm was also observed in the AFM images (Fig. 4). Considering the agreement among the $FWHM_{2\theta}$, XRR and AFM results, it could be concluded that, at as deposited and after nine cycles of hydrogen loading and unloading, the fraction of lattice defects was relatively small. Therefore, although a large number of lattice defects were introduced into the lattice during the initial hydrogen loading cycles, further hydrogen loading and unloading cycles resulted in the sweeping of such defects to the grain boundary between the α- and β-phase grains (denoted as 'α–β grain boundary') together with in-plane grain growth. The intensity increase after several hydrogen cycles also supports this conclusion. Except for the phase transformation period, the FWHM along the χ direction at ψ = 0° corresponds mainly to the fluctuation of the [111] direction (Fig. 10*d*, ψ = 0°). Thus, the observed gradual decrease (∼0.8°) in the $FWHM_{\chi}$ suggests that a decrease in the [111] direction fluctuation, or (111) texture enhancement, most likely occurs together with in-plane crystal growth during the hydrogen loading and unloading cycles. Note that the increase in the in-plane grain size also results in an $FWHM_{\chi}$ decrease; however, its effect would be relatively small, since the $FWHM_{2\theta}$ decrease at ψ = 70.5° is only ∼0.3°. The FWHM along the χ direction at ψ = 70.5° is also related mainly to the fluctuation of the [111] direction and the observed decrease (∼1°) again indicates (111) texture enhancement (Fig. 10*d*, ψ = 70.5°).

In summary, it is clear that the cyclic hydrogen loadings resulted in in-plane grain growth, lattice defect removal and (111) texture improvement. Consequently, a peak intensity (height) increase was also observed. Accordingly, from the viewpoint of the in-plane stress in the film, we discuss the evolution mechanism in the next section.

3.3. Film structure evolution mechanism

To investigate the film structure evolution mechanism, the stress and the strain-free lattice parameter in the film were estimated using a diffraction stress analysis. Fig. 11 shows the analysis procedure and the relation with the phenomena during the hydrogen loading. During the hydrogen loading (the left column of Fig. 11), owing to the hydrogen incorporation into the lattice, the lattice parameter increases. In addition, a large in-plane compressive stress would be induced, since the film is clamped to the substrate, and stress relaxation may take place. The combination of these two components, *i.e.* the increase in the lattice parameter and the in-plane stress, results in a tilt angle (ψ)-dependent lattice spacing change. Thus, it is impossible to calculate the in-plane stress in a simple way, such as an estimation of the in-plane stress simply from the out-of-plane lattice spacing change. Instead, the ψ-dependent lattice spacing change should be analysed in terms of the diffraction stress analysis (the right column of Fig. 11). In this study, since the film is (111) textured, two (111) lattice spacings at ψ = 0 and 70.5° were measured. Thereafter, using the diffraction stress analysis, these two spacings were converted (separated) into two components: one is the strain-free lattice parameter and the other is the in-plane stress. The former component corresponds to the hydrogen-induced lattice parameter increase. Note that, in this study, the frequently employed assumption that the strain-free lattice parameter equals the bulk lattice parameter was not adopted; instead, the strain-free lattice parameter remained variable rather than being constant.

Under the assumption of rotationally symmetric biaxial stress ($\sigma_{11} = \sigma_{22} = \sigma_{\parallel}$ and $\sigma_{33} = 0$, where σ_{11} and σ_{22} are the in-plane stresses and σ_{33} is the out-of-plane stress), the strain at the tilt angle ψ for the (111)-textured cubic crystal structure thin film can be written as (Hauk, 1997; Tanaka *et al.*, 1999;

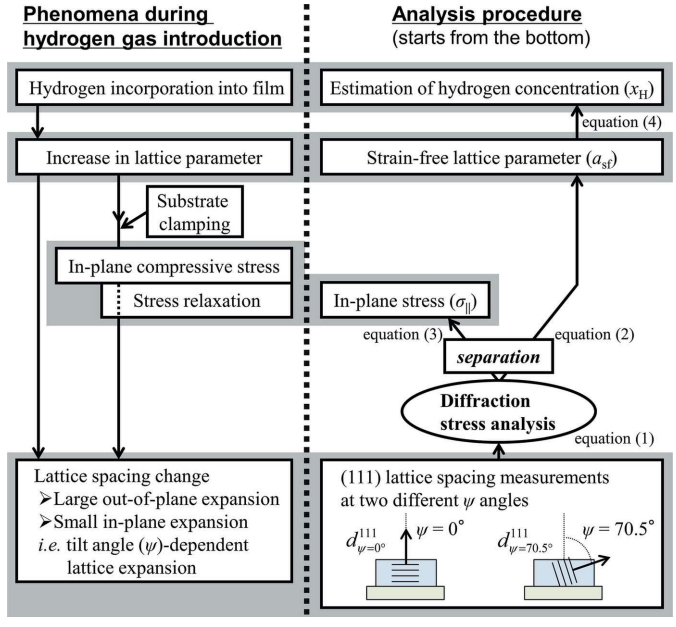

Figure 11
Relation between the phenomena during the hydrogen loading and the analysis procedure. The diffraction stress analysis was independently conducted for each of the α and β phases, *i.e.* the analysis was performed two times when the α and β phases coexist in the film.

Kamminga *et al.*, 2000; Leoni *et al.*, 2001; Welzel *et al.*, 2005; Yokoyama & Harada, 2009; Harumoto *et al.*, 2014)

$$\varepsilon_{\psi}^{111} = \frac{d_{\psi}^{111} - a_{\rm sf}/3^{1/2}}{a_{\rm sf}/3^{1/2}} = \left(2S_1^{111} + \tfrac{1}{2}S_2^{111}\sin^2\psi\right)\sigma_{||}, \qquad (1)$$

where d_{ψ}^{111} is the (111) lattice spacing at the tilt angle ψ and $a_{\rm sf}$ is the strain-free lattice parameter. S_1^{111} and $\frac{1}{2}S_2^{111}$ are the diffraction elastic constants for the (111)-textured thin film and can be described as $(1/3)s_{11} + (2/3)s_{12} - (1/6)s_{44}$ and $(1/2)s_{44}$, respectively, where s_{11}, s_{12} and s_{44} are the single-crystal elastic compliances. Employing the compliances in the literature (Hsu & Leisure, 1979) (s_{11} = 13.744 TPa^{-1}, s_{12} = −5.995 TPa^{-1} and s_{44} = 14.035 TPa^{-1} for pure Pd; s_{11} = 12.923 TPa^{-1}, s_{12} = −5.507 TPa^{-1} and s_{44} = 15.760 TPa^{-1} for $PdH_{0.66}$), the two constants S_1^{111} and $\frac{1}{2}S_2^{111}$ were calculated as −1.754 and 7.018 TPa^{-1} for the α phase, and −1.991 and 7.880 TPa^{-1} for the β phase ($PdH_{0.66}$). Since the actual hydrogen concentration varies in the range from pure Pd to $PdH_{0.66}$, the errors shown in Table S1 (in the supplementary information) were introduced into the diffraction elastic constants and they were employed during the calculation of error bars. Note that the effects of defects and size on the diffraction elastic constants would be negligibly small in comparison with the introduced (relatively large) errors listed in Table S1.

Equation (1) can be solved analytically using the (111) lattice spacings at ψ = 0 and 70.5° ($d_{\psi=0^\circ}^{111}$ and $d_{\psi=70.5^\circ}^{111}$) as follows (Harumoto *et al.*, 2017):

$$a_{\rm sf} = 3^{1/2}\left[\left(\frac{9}{4}\frac{S_1^{111}}{\frac{1}{2}S_2^{111}} + 1\right)d_{\psi=0^\circ}^{111} - \frac{9}{4}\frac{S_1^{111}}{\frac{1}{2}S_2^{111}}d_{\psi=70.5^\circ}^{111}\right], \qquad (2)$$

$$\sigma_{||} = -\frac{9}{2}\frac{d_{\psi=0^\circ}^{111} - d_{\psi=70.5^\circ}^{111}}{\left(9S_1^{111} + 4\frac{1}{2}S_2^{111}\right)d_{\psi=0^\circ}^{111} - 9S_1^{111}d_{\psi=70.5^\circ}^{111}}. \qquad (3)$$

Note that $\sin^2 70.5^\circ$ was assumed to be 8/9. Employing the (111) lattice spacings calculated from the peak centre positions ($2\theta_c$) at ψ = 0 and 70.5°, the strain-free lattice parameter and the in-plane stress were calculated (Fig. 12). The strain-free lattice parameter was also employed to estimate the hydrogen concentration ($x_{\rm H}$), or the H/Pd atomic ratio. Since it has been separated into the two components of the strain-free lattice parameter and the in-plane stress, it is possible to estimate the hydrogen concentration from the strain-free lattice parameter even if a large stress exists and stress relaxation takes place. The following relation between the lattice parameter and the hydrogen concentration was adopted (Peisl, 1978; Manchester *et al.*, 1994; Wagner *et al.*, 2016; Wagner & Pundt, 2016; Harumoto *et al.*, 2017):

$$\frac{a_{\rm sf} - a_{\rm bulk\ Pd}}{a_{\rm bulk\ Pd}} = \alpha_{\rm H}x_{\rm H}, \qquad (4)$$

where $\alpha_{\rm H}$ and $a_{\rm bulk\ Pd}$ are the expansion coefficient (0.061) and the bulk lattice parameter of pure Pd (0.3890 nm, PDF No. 00-046-1043). Note that this equation is valid not only for the α phase but also for the β phase. The hydrogen concentration axis was added to the right-hand side of Fig. 12(*a*).

Before the hydrogen gas introduction (t = 0 to 1.2 h), the strain-free lattice parameter was equal to the bulk one and the in-plane stress in the film was almost zero, indicating almost no residual stress and $x_{\rm H}$ = 0. [More specifically, the lattice parameter was slightly larger than the bulk one and the stress was slightly compressive, although these deviations were within the error. They could be attributed to the atomic peening effect, which results in lattice expansion and

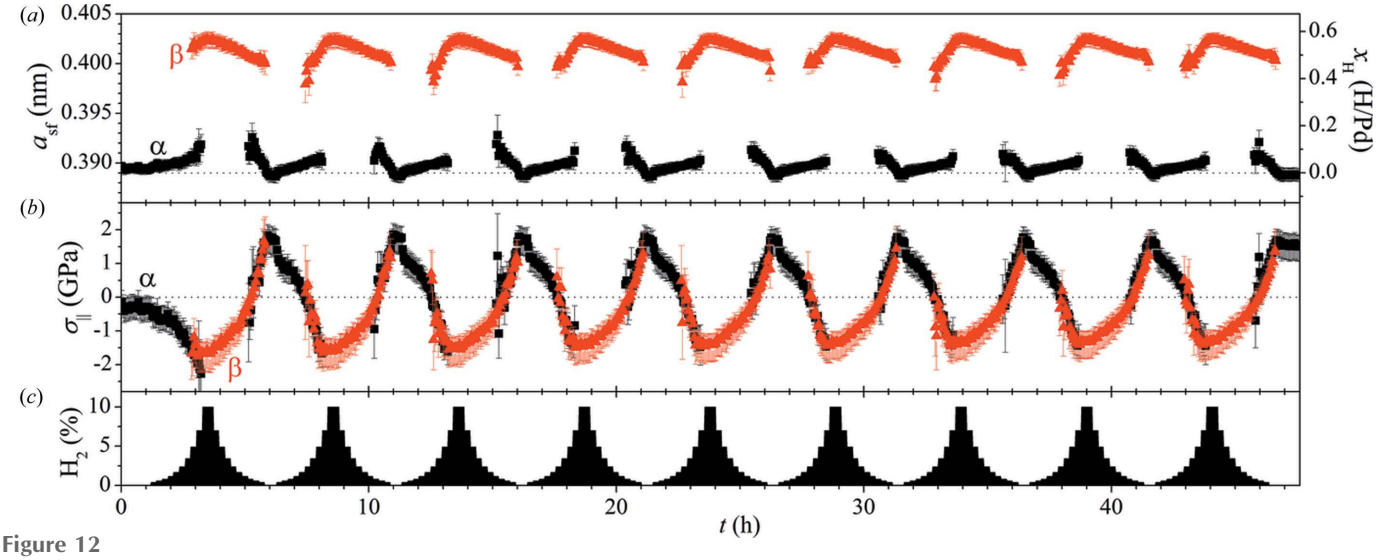

Figure 12
Profiles for (*a*) strain-free lattice parameter ($a_{\rm sf}$) and (*b*) in-plane stress ($\sigma_{||}$). In (*a*), the axis for the hydrogen concentration ($x_{\rm H}$) is shown on the right-hand side. The dotted line in (*a*) denotes the lattice parameter of the bulk Pd, or $x_{\rm H}$ = 0. The black square and red triangle plots correspond to the results of the α and β phases, respectively. The introduced hydrogen gas profile is shown in (*c*).

compressive stress, during the sputter deposition (Hoffman & Thornton, 1982).]

The hydrogen loading (from t = 1.2 h) resulted in both lattice expansion and large in-plane compressive stress. The gap in the strain-free lattice parameter (*i.e.* the difference in hydrogen concentration) between the α and β phases corresponds to the miscibility gap in the phase diagram of the Pd–H system (Fig. 12*a*). The hydrogen solubility limit in the α phase at the first hydrogen introduction cycle was around $x_H = 0.1$ (at $t = 3.2$ h). This x_H value is very much larger than the bulk case ($x_H = 0.02$) (Manchester *et al.*, 1994); however, it is very close to the value reported for a 32 nm Pd nanocube ($x_H = 0.15$) in the literature (Bardhan *et al.*, 2013: Griessen *et al.*, 2016). This suggests that the α-to-β transformation took place under a size effect, namely the narrowing of the miscibility gap at nanometre-sized grains (Feenstra *et al.*, 1983; Eastman *et al.*, 1993). The hydrogen concentration of the β phase during the initial formation ($t = 2.9$ h) was around $x_H = 0.52$ and increased up to $x_H = 0.55$ at 10% hydrogen gas (t = 3.3−3.7 h).

Unlike the results for the strain-free lattice parameters, there was no gap between the in-plane stresses of the α and β phases (Fig. 12*b*). Instead, the plots of the two phases overlap and are almost connected with each other within the error range. This indicates that the formation and the grain growth of the β phase took place under the same in-plane compressive stress that the α phase receives. The maximum compressive stress during the first hydrogen gas introduction was around −2 GPa. This stress value is in good agreement with that measured by the substrate curvature (Leervad Pedersen *et al.*, 2004; Pundt & Kirchheim, 2006; Kirchheim & Pundt, 2014; Wagner *et al.*, 2016; Wagner & Pundt, 2016). The large in-plane compressive stress corresponds to the presence of the substrate clamping effect, which suppresses the in-plane lattice expansion (Miceli *et al.*, 1991; Reimer *et al.*, 1993; Zabel & Weidinger, 995; Laudahn *et al.*, 1999; Pundt & Kirchheim, 2006; Pivak *et al.*, 2011; Wagner *et al.*, 2011; Kirchheim & Pundt, 2014; Callori *et al.*, 2016; Harumoto *et al.*, 2017). Furthermore, this stress value also suggests that stress relaxation, namely plastic deformation, took place during the hydrogen loading, since this compressive stress (−2 GPa) is smaller than the estimated value under no plastic deformation [−9.9 GPa at $x_H = 0.55$, calculated from the ratio between the in-plane stress and hydrogen concentration, $\sigma_{||}/x_H = -18$ GPa, for (111)-textured Pd films under no plastic deformation] (Wagner *et al.*, 2016; Wagner & Pundt, 2016; Harumoto *et al.*, 2017).

During the hydrogen unloading (from $t = 3.7$ h), a decrease in the hydrogen concentration of the β phase was initially observed. After the decrease of x_H, transformation from the β phase to the α phase took place and was completed when the β-phase hydrogen concentration was 0.46. This value is smaller than that at formation ($x_H = 0.52$) and corresponds to hysteresis during the transformation (Pundt & Kirchheim, 2006; Lee *et al.*, 2010; Pivak *et al.*, 2011; Bardhan *et al.*, 2013; Baldi *et al.*, 2014; Griessen *et al.*, 2016). The hydrogen concentration of the α phase at formation was around 0.1 and in agreement with that at the α-to-β transformation. Without hydrogen gas introduction (t = 5.8−6.3 h), the strain-free lattice parameter returned to the initial value (*i.e.* the bulk value), indicating $x_H = 0$.

In addition to the decrease in x_H, the large compressive stress in the β phase was released during hydrogen unloading. Similar to the α-to-β transformation, the β-to-α transformation also took place under the same in-plane stress present in the β phase. After the completion of the β-to-α transformation, the stress in the film did not return to its initial value ($\sigma_{||} \simeq 0$ at $t = 0$ h), instead exhibiting a large tensile stress ($\sigma_{||} \simeq 1.8$ GPa). This also indicates that plastic deformation at the Pd film/APA underlayer interface took place during the first hydrogen loading and unloading.

During the second and subsequent hydrogen loading and unloading cycles (from $t = 6.3$ h), the hydrogen concentration plots exhibited similar tendencies to the first cycle. However, under closer examination, the solubility limit in the α phase decreased compared with the first cycle. This could be attributed to the effect of the increased in-plane grain size, which resulted in the widening of the miscibility gap (Feenstra *et al.*, 1983; Eastman *et al.*, 1993). The hydrogen concentration of the β phase at the initial stage of formation was decreased from $x_H = 0.52$ (in the first cycle) to $x_H = 0.45$ (the average of the second and later cycles). This decrease in x_H of the β phase at formation could be explained by the effect of stress on the thermodynamic properties (Pivak *et al.*, 2009, 2011; Wagner & Pundt, 2016), rather than the increase in grain size. Indeed, the in-plane stress at the β-phase formation of the first cycle was a large compressive stress of $\sigma_{||} \simeq -1$ GPa, while those of the second and subsequent cycles were around zero (Fig. 12*b*). Also, in the β phase, the rate of increase of x_H at hydrogen loading was larger than the rate of decrease of x_H at unloading. In contrast, in the α phase, the rate of increase of x_H was smaller than the rate of decrease of x_H. Although the details are under investigation, these effects could be attributed to hysteresis during the transformation (Pundt & Kirchheim, 2006; Lee *et al.*, 2010; Pivak *et al.*, 2011; Bardhan *et al.*, 2013; Baldi *et al.*, 2014; Griessen *et al.*, 2016). Note that no obvious changes in $\sigma_{||}$ and x_H were detected between the second and subsequent cycles, while large changes were observed between the first and second cycles.

In light of these results, we discuss the mechanism of film structure evolution during hydrogen loading and unloading cycles. We consider that the main result observed is the following:

During the α-to-β phase transformation, the formation and grain growth of the β phase took place under the same in-plane stress present in the α phase, and *vice versa*.

This suggests that the growth of the β-phase grain during the α-to-β transformation occurred in plane rather than out of plane. This is because the in-plane grain growth mode is able to take place under the above conditions (Figs. 13*b*–13*d*), while out-of-plane grain growth promotes a stress difference between the α and β phases (Fig. 13*a*). From the viewpoint of the grain boundary between the α and β phases (α–β grain boundary), transformation under the in-plane growth mode can be recognized as in-plane α–β grain boundary motion

taking place during hydrogen loading cycles. Since the grain boundary between two α phases (α–α grain boundary) would have higher energy (owing to the interfacial energy) than the inside of the α-phase grain, the β-phase grain which is growing in the α-phase grain can take over such a region readily and grow over the α–α grain boundary, resulting in a change in the grain structure during the cyclic α–β grain boundary motion. Such motion can result in in-plane grain growth and (111) texture improvement, as the film can simply minimize its energy by reducing the α–α and α–β grain boundaries and depositing the stable (111) plane on the film surface. Also, the cyclic α–β grain boundary motion can sweep the lattice defects to the α–β grain boundary, resulting in the removal of lattice defects from the inside of the lattice. It should be noted that, in the case of Nb films, the in-plane grain growth mode of the hydride phase has been reported already (Nörthemann & Pundt, 2008).

These findings also suggest that the evolution based on this mechanism takes place only for thin films and not thick films or the bulk case. Indeed, in the case of thick Pd films of thickness 1080 nm in the literature (Čížek *et al.*, 2013), the (111) texture was degraded by hydrogen loading.

In summary, from the observed agreement of in-plane stresses between α and β phases, we have described a mechanism of film structure evolution. It was concluded that the cyclic in-plane α–β grain boundary motion during phase transformation was the origin of the observed film structure evolution.

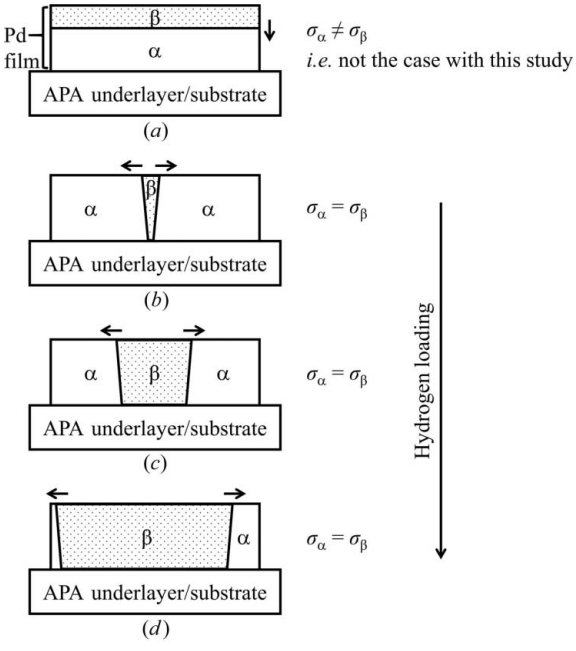

Figure 13
Schematic illustrations of the α-to-β phase transformation in (111)-textured Pd thin films. (*a*) The out-of-plane grain growth mode and (*b*–*d*) the in-plane grain growth mode. The in-plane stresses in the α and β phases are denoted as σ_α and σ_β, respectively. In (*b*–*d*), since the α and β phase grains compete with each other, the in-plane stresses in two phases should be equalized. In the case of hydrogen unloading, all arrows in the illustrations should be reversed.

4. Conclusions

We performed an *in situ* X-ray diffraction study on a Pd thin film under hydrogen loading and unloading cycles. It was confirmed that, in the case of the (111)-textured Pd thin film, the hydrogen loading and unloading cycles resulted in grain growth rather than refinement. Also, the film texture improved during cycles. Hence, changes in the film structure during the hydrogen loading and unloading cycles differed from the bulk case. Accordingly, by employing diffraction stress analysis, the mechanism of grain growth and texture improvement was found. On the basis of the observed agreement of in-plane stresses between the α and β phases, it was concluded that grain growth during the α-to-β and β-to-α phase transformations took place mainly along the in-plane direction, leading to film structure evolution in in-plane grain growth, lattice defect removal and (111) texture enhancement. We believe that this study facilitates the use of hydrogen for the post-deposition process in thin metal films.

Acknowledgements

The AES depth profiles were measured under the support of Dr M. Tada, Materials Analysis Division, Tokyo Institute of Technology.

Funding information

The authors are thankful for financial support from the Japan Society for the Promotion of Science (JSPS) Grants-in-Aid for Scientific Research (KAKENHI) (Nos. 25870772 and 16K14372.

References

Baldi, A., Narayan, T. C., Koh, A. L. & Dionne, J. A. (2014). *Nat. Mater.* **13**, 1143–1148.
Bardhan, R., Hedges, L. O., Pint, C. L., Javey, A., Whitelam, S. & Urban, J. J. (2013). *Nat. Mater.* **12**, 905–912.
Callori, S. J., Rehm, C., Causer, G. L., Kostylev, M. & Klose, F. (2016). *Metals*, **6**, 125.
Čížek, J., Melikhova, O., Vlček, M., Lukáč, F., Vlach, M., Procházka, I., Anwand, W., Brauer, G., Mücklich, A., Wagner, S., Uchida, H. & Pundt, A. (2013). *Int. J. Hydrogen Energy*, **38**, 12115–12125.
Eastman, J. A., Thompson, L. J. & Kestel, B. J. (1993). *Phys. Rev. B*, **48**, 84–92.
Feenstra, R., de Bruin-Hordijk, G. J., Bakker, H. L. M., Griessen, R. & de Groot, D. G. (1983). *J. Phys. F Met. Phys.* **13**, L13–L18.
Flanagan, T. B. & Noh, H. (1995). *J. Alloys Compd.* **231**, 1–9.
Gremaud, R., Gonzalez-Silveira, M., Pivak, Y., de Man, S., Slaman, M., Schreuders, H., Dam, B. & Griessen, R. (2009). *Acta Mater.* **57**, 1209–1219.
Griessen, R., Strohfeldt, N. & Giessen, H. (2016). *Nat. Mater.* **15**, 311–317.
Harris, I. R. & McGuiness, P. J. (1991). *J. Less-Common Met.* **172–174**, 1273–1284.
Harumoto, T., Ohnishi, Y., Nishio, K., Ishiguro, T., Shi, J. & Nakamura, Y. (2017). *AIP Adv.* **7**, 065108.
Harumoto, T., Sannomiya, T., Matsukawa, Y., Muraishi, S., Shi, J., Nakamura, Y., Sawada, H., Tanaka, T., Tanishiro, Y. & Takayanagi, K. (2013). *J. Appl. Phys.* **113**, 084306.
Harumoto, T., Sannomiya, T., Muraishi, S., Shi, J. & Nakamura, Y. (2014). *J. Appl. Cryst.* **47**, 1490–1501.

Harumoto, T., Sannomiya, T., Muraishi, S., Shi, J. & Nakamura, Y. (2016). *J. Appl. Cryst.* **49**, 909–917.
Hauk, V. (1997). Editor. *Structural and Residual Stress Analysis by Nondestructive Methods.* Amsterdam: Elsevier.
Hayashi, E., Kurokawa, Y. & Fukai, Y. (1998). *Phys. Rev. Lett.* **80**, 5588–5590.
Hoffman, D. W. & Thornton, J. A. (1982). *J. Vac. Sci. Technol.* **20**, 355–358.
Hsu, D. K. & Leisure, R. G. (1979). *Phys. Rev. B*, **20**, 1339–1344.
Iwaki, T., Kuriiwa, T., Kamegawa, A., Takamura, H. & Okada, M. (2009). *Mater. Trans.* **50**, 499–505.
Kamminga, J.-D., de Keijser, Th. H., Mittemeijer, E. J. & Delhez, R. (2000). *J. Appl. Cryst.* **33**, 1059–1066.
Kirchheim, R. & Pundt, A. (2014). *Physical Metallurgy*, Vol. III, 5th ed., edited by D. E. Laughlin & K. Hono, ch. 25. Amsterdam: Elsevier.
Laudahn, U., Pundt, A., Bicker, M., von Hülsen, U., Geyer, U., Wagner, T. & Kirchheim, R. (1999). *J. Alloys Compd.* **293–295**, 490–494.
Lee, E., Lee, J. M., Koo, J. H., Lee, W. & Lee, T. (2010). *Int. J. Hydrogen Energy*, **35**, 6984–6991.
Leervad Pedersen, T. P., Liesch, C., Salinga, C., Eleftheriadis, T., Weis, H. & Wuttig, M. (2004). *Thin Solid Films*, **458**, 299–303.
Leoni, M., Welzel, U., Lamparter, P., Mittemeijer, E. J. & Kamminga, J. D. (2001). *Philos. Mag. A*, **81**, 597–623.
Manchester, F. D., San-Martin, A. & Pitre, J. M. (1994). *J. Phase Equilib.* **15**, 62–83.
Miceli, P. F., Zabel, H., Dura, J. A. & Flynn, C. P. (1991). *J. Mater. Res.* **6**, 964–968.
Murakami, Y., Kanezaki, T. & Mine, Y. (2010). *Metall. Mater. Trans. A*, **41**, 2548–2562.
Nakayama, R. & Takeshita, T. (1993). *J. Alloys Compd.* **193**, 259–261.
Noh, H., Flanagan, T. B., Cerundolo, B. & Craft, A. (1991). *Scr. Metall. Mater.* **25**, 225–230.
Noh, H., Flanagan, T. B. & Ransick, M. H. (1992). *Scr. Metall. Mater.* **26**, 353–358.
Nörthemann, K. & Pundt, A. (2008). *Phys. Rev. B*, **78**, 014105.
Okada, M., Kamegawa, A., Nakahigashi, J., Yamaguchi, A., Fujita, A. & Yamauchi, M. (2010). *Mater. Sci. Eng. B*, **173**, 253–259.
Peisl, H. (1978). *Hydrogen in Metals I*, edited by G. Alefeld & J. Völkl, ch. 3. Berlin: Springer-Verlag.
Pivak, Y., Gremaud, R., Gross, K., Gonzalezsilveira, M., Walton, A., Book, D., Schreuders, H., Dam, B. & Griessen, R. (2009). *Scr. Mater.* **60**, 348–351.
Pivak, Y., Schreuders, H., Slaman, M., Griessen, R. & Dam, B. (2011). *Int. J. Hydrogen Energy*, **36**, 4056–4067.
Pundt, A. & Kirchheim, R. (2006). *Annu. Rev. Mater. Res.* **36**, 555–608.
Reimer, P. M., Zabel, H., Flynn, C. P., Matheny, A., Ritley, K., Steiger, J., Blässer, S. & Weidinger, A. (1993). *Z. Phys. Chem.* **181**, 367–373.
Sidorenko, V. M., Fedorov, V. V., Barabash, L. V. & Pokhmurskii, V. I. (1978). *Mater. Sci.* **13**, 607–610.
Tanaka, K., Akiniwa, Y., Ito, T. & Inoue, K. (1999). *Jpn. Soc. Mech. Eng. Int. J. Ser. A*, **42**, 224–234.
Wagner, S., Kramer, T., Uchida, H., Dobron, P., Cizek, J. & Pundt, A. (2016). *Acta Mater.* **114**, 116–125.
Wagner, S. & Pundt, A. (2016). *Int. J. Hydrogen Energy*, **41**, 2727–2738.
Wagner, S., Uchida, H., Burlaka, V., Vlach, M., Vlcek, M., Lukac, F., Cizek, J., Baehtz, C., Bell, A. & Pundt, A. (2011). *Scr. Mater.* **64**, 978–981.
Watanabe, K., Okuma, N., Fukai, Y., Sakamoto, Y. & Hayashi, Y. (1996). *Scr. Mater.* **34**, 551–557.
Welzel, U., Ligot, J., Lamparter, P., Vermeulen, A. C. & Mittemeijer, E. J. (2005). *J. Appl. Cryst.* **38**, 1–29.
Yokoyama, R. & Harada, J. (2009). *J. Appl. Cryst.* **42**, 185–191.
Zabel, H. & Weidinger, A. (1995). *Comments Cond. Mater. Phys.* **17**, 239–262.